FEMTA micropropulsion system characterization by DSMC

Cite as: AIP Conference Proceedings **2132**, 070006 (2019); https://doi.org/10.1063/1.5119560
Published Online: 05 August 2019

Shashank Jaiswal, Israel B. Sebastião, Andrew Strongrich, and Alina A. Alexeenko

FEMTA Micropropulsion System Characterization by DSMC

Shashank Jaiswal[1], Israel B. Sebastião[1], Andrew Strongrich[1] and Alina A. Alexeenko[1,a)]

[1]*School of Aeronautics & Astronautics, Purdue University, West Lafayette, IN 47907, USA*

[a)]Corresponding author: alexeenk@purdue.edu

Abstract. CubeSats with compact, low-power attitude-control systems open up opportunities for deep-space missions as well as cost-effective constellation-based satellites targeting remote sensing and communication applications. Film Evaporation MEMS Tunable Array (FEMTA) is a micropropulsion technology that employs thermally-controlled surface tension in a microscale capillary for vaporization of liquid water propellant. FEMTA thrusters generate tunable thrust on the order of micro-newton with a thrust-to-power ratio of about 230 $\mu N/W$. Because of the small scale capillary on the order of 10 micron and below, the rarefied flow effects are significant for the vapor flow in this system. In the present work, the direct simulation Monte Carlo (DSMC) SPARTA solver is used to numerically evaluate two key aspects of the FEMTA system: a) the evaporation of the propellant in the quiescent system-state, i.e., without heaters actuation, and b) effect of plume expansion on the CubeSat walls to inform thrust cell placement and estimate the extent of plume contamination. Both factors affect the propellant consumption and system lifetime.

INTRODUCTION

Modularity, maneuverability, maintainability, lifetime, autonomous operation, and launch/hardware cost mainly dictate the design of small satellites [1]. In the vacuum of space, and at the scale of pico/nano satellites, thrusts on order of micro-newtons can be very well exploited for maneuverability and attitude control. Several micro-propulsion technologies are currently being explored, including, ion [2], Hall [3], field emission electric propulsion (FEEP) [4], cold gas chemical micropropulsion [5], radio-frequency gas-discharge (RFGD) [6], and water vapor based Film-evaporation MEMS Tunable Array [7]. In particular, FEMTA employs thermally-controlled surface tension in a microscale capillary for vaporization of liquid water propellant, and generates tunable thrust on the order of micro-newton with a thrust-to-power ratio of about 230 $\mu N/W$. A comprehensive comparison of SmallSat propulsion systems based on specific impulse, thrust, power, and size can be found in [6, 7].

In the present work, we will focus on characterizing FEMTA flow structure using the direct simulation Monte Carlo (DSMC) method. DSMC is a widely used stochastic approach for solution of the integro-differential Boltzmann equation for gas flows [8] by Monte Carlo evaluation of trajectories of N-particle systems. In the present era, DSMC finds application in for solving rarefied gas flow problems encountered in high-altitude hypersonic aerothermodynamics [9], heat and mass transfer in FEMTA [10], vacuum technology [11], planetary sciences [12], RFGD microthruster [6], etc.

Specifically in the current work, DSMC is used to numerically evaluate two key aspects of the FEMTA system: a) the evaporation of the propellant in the quiescent system-state, i.e., without heaters actuation, and b) effect of thruster plumes on the CubeSat walls to inform thrust cell placement. Both factors affect the propellant consumption and system lifetime. In the quiescent state, with no heating and no-shutter, the evaporation dominates. By the numerical modeling we quantitatively address the impact of shutter geometry on the vapor pressure in the liquid/vapor meniscus region and the overall vapor mass flow rate; condensation; and the effect of thruster plume on CubeSat walls. In the section that follows, we give a brief overview of FEMTA thruster, and 1U CubeSat for plume contamination studies. Section 3 presents the results for the quiescent evaporation, condensation, and plume contamination problems. Concluding remarks are given in Section 4.

31st International Symposium on Rarefied Gas Dynamics
AIP Conf. Proc. 2132, 070006-1–070006-12; https://doi.org/10.1063/1.5119560
Published by AIP Publishing. 978-0-7354-1874-5/$30.00

FEMTA Micro-propulsion

FEMTA exploits microscale effects in which fluid surface tension acts as a thermal valve, thereby creating a very simple propulsion and thermal management system for SmallSat applications. FEMTA capitalizes on the microscale properties of water surface tension, fluid film temperature, and vapor pressure. There is a critical capillary gap size where the surface tension of the fluid is balanced with the internal pressure of the fluid exposed to a vacuum. If the nozzle dimension is less than this critical capillary gap size, then raising the film temperature of the meniscus allows the vapor pressure at the meniscus to rise, upsetting this equilibrium and initiating vacuum boiling. Adjusting the temperature of the meniscus allows for a controlled, micronewton scale thrust vector. From a propulsive performance viewpoint, FEMTA generates thrust up to $70\,\mu N$ per nozzle at less than $0.1\ W$, thrust to power ratio of $250\,\mu N/W$, and specific impulse (I_{sp}) of 80 seconds [7, 13, 14].

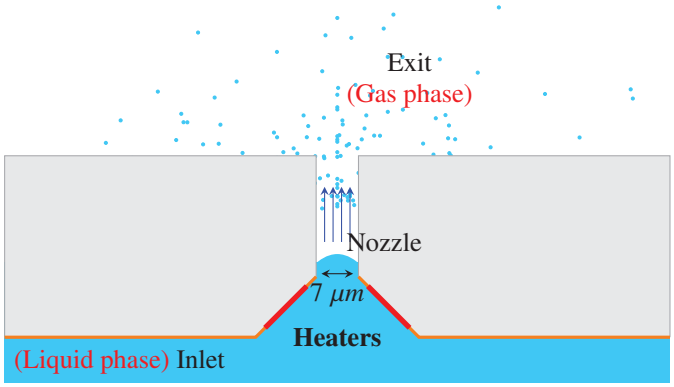

FIGURE 1: Schematic of FEMTA GEN4 MEMS devices (not to scale).

The design of the FEMTA thruster is based on a 2D converging-diverging nozzle created using several sequences of etching and material deposition on a <1, 0, 0> oriented silicon wafer. A cutout view of the nozzle geometry can be seen in Fig. (1). In the figure the silicon wafer is light gray, a layer of silicon oxide for insulation is orange, the platinum heaters are red and the propellant (water) is blue. The throat height and throat length of the nozzle are approximately 7 and 30 μm, respectively, whereas the out of plane dimension of the nozzle is approximately $2.5\,mm$ [14]. The heaters are placed in close proximity to the meniscus to increase evaporative mass flux. After evaporation, the water vapor is expanded out of the nozzle to create thrust. Details about previous generations of FEMTA as well as the associated fabrication process can be found in [13].

Figure (2) illustrates a 1U-CubeSat ($100 \times 100 \times 100\ mm^3$) with four FEMTA thrusters. Consider the simplified 2-D schematic: when the top and the bottom thrusters are activated, the CubeSat will rotate in clockwise direction to the viewing plane; and when the left and right thrusters are activated, the CubeSat will rotate in counter-clockwise direction. Extensive details about 1U-CubeSat and FEMTA thrusters can be found in [7, 10, 13, 14].

RESULTS AND DISCUSSIONS

Because of the small scale capillary on the order of 10 micron and below, the rarefied flow effects are significant for the vapor flow in this system. In the present section, we numerically evaluate the evaporation of the propellant in the quiescent system-state, i.e., without heaters actuation, and the effect of plume expansion on the CubeSat walls. SPARTA [15] has been employed for carrying out DSMC simulations in the present work. It implements the DSMC method as proposed by Bird [8]. Herein, given the temperature range of interest, only translational and rotational energy modes are considered. The solver has been benchmarked [15] and widely used for studying hypersonic, subsonic and thermal [16, 17, 18, 19, 20, 21] gas flow problems. In particular, SPARTA relying on C++ object oriented design, has been shown to perform very well on massively parallel architectures [15, 16]. In this work, cell size less than $\lambda/3$ has been ensured in all the test cases. A minimum of 30 DSMC simulator particles per cell are used in conjunction with the no-time collision (NTC) algorithm. Each steady-state simulation has been averaged for a minimum 100,000 samples, each taken at every time step, so as to minimize the statistical noise.

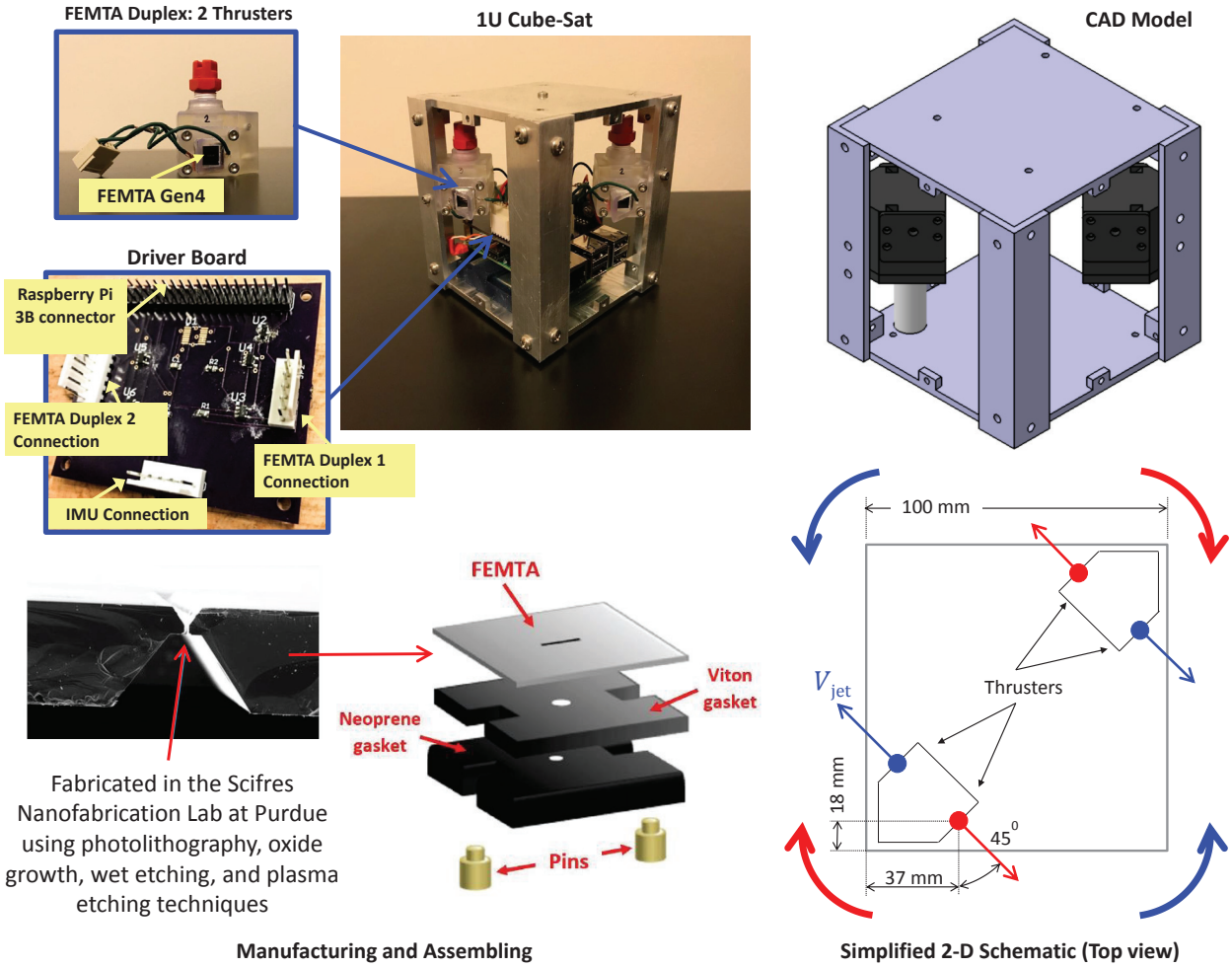

FIGURE 2: Overall FEMTA description (adapted from [14]).

Evaporation in Quiescent State

A two-dimensional simplified schematic of FEMTA thruster has been illustrated in Fig. (3). Using the thermally-controlled surface tension (via heaters) in the microscale capillary, the liquid water propellant is vaporized–which in turn generates tunable thrust on the order of micro-newtons [7]. A simple, yet effective design, requires use of a shutter at the exit to prevent the water vapors evaporating to the vacuum (of space) during the nozzle quiescent state. It is worth emphasizing that the entire thruster is in scale of micro-meters and therefore the use of a simple shutter makes the overall design, fabrication, and mass-production relatively easier. By the numerical modeling we quantitatively address the impact of shutter geometry on the vapor pressure in the liquid/vapor meniscus region and the overall vapor mass flow rate.

The schematic of the simulation geometry–denoted by red dashed lines–has been shown in Fig. (3). The water vapor molecules with mean-velocity of 0 m/s enter the domain at the bottom from the thruster outlet, pass through the gap between the shutter and bimetallic elements, and expand into the vacuum. In the present case, we consider two geometric variables: a) w: half-width of the shutter, and b) g: gap between the shutter and bimetallic-elements. The shutter and the thruster walls are kept at a temperature of 298 K.

A simulation domain of $250\,\mu m \times 250\,\mu m$ is first discretized uniformly using 250×250 cell Cartesian-grid, which results in a uniform cell size of $1\,\mu m$. Assuming the cells are numbered starting from the bottom-left meniscus region, we subdivide each of the first 15×35 parent cells into 10×10 child cells. This is done so as to resolve the flow in the near shutter region.

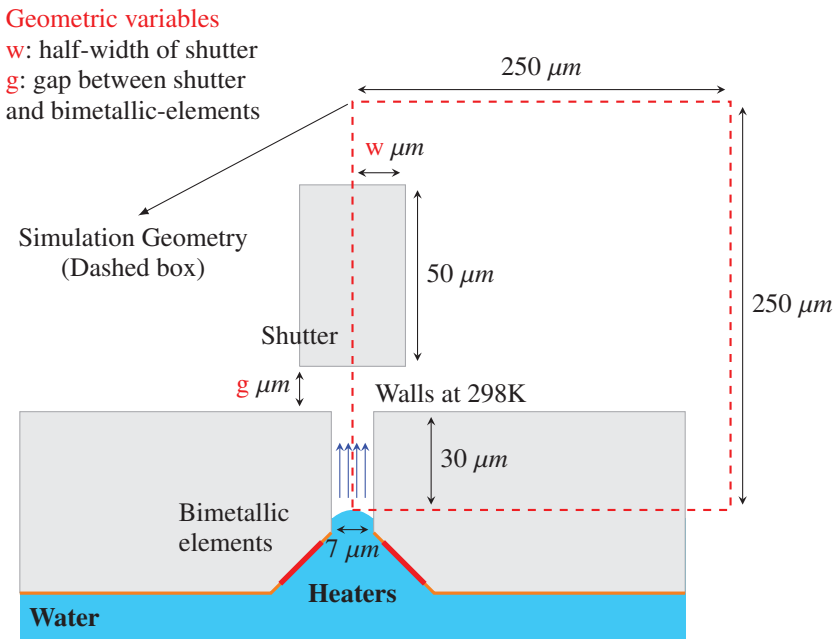

FIGURE 3: Numerical setup for quantifying evaporation in quiescent system state.

Quantity	Value
Inlet flow velocity, (m/s)	0
Inlet flow temperature, (K)	298
Working Fluid	H_2O at 273.15 K
Wall temperature, $T_w(K)$	298
Average Cell Size (μm)	1
Timestep, Δt (s)	10^{-9}
Average particles per cell	30

TABLE 1: Common case parameters for quantification of evaporation in quiescent FEMTA system state.

Parameter	Case 1	Case 2	Case 3	Case 4
Mass flow rate, $\dot{m}$ $(\mu g/s)$	10	20	30	40
Number density, n $(10^{23} m^{-3})$	1.3	2.6	3.9	5.2
$\approx$ Mean free path, λ (μm)	8	4	2.67	2

TABLE 2: Parameters for different flow rate conditions. Half-width (w), and shutter-gap (g) are varied for each of these cases.

The DSMC simulation parameters have been indicated in the Tabs. (1,2). At walls, we use fully diffuse surface boundary condition. At the top and right free-stream boundaries, the outlet boundary condition has been used. At the bottom boundary, an inlet boundary condition is imposed with gas molecules entering at $0\,m/s$ mean velocity and the specified number density. At the left boundary, a symmetry/fully specular boundary condition is applied. The simulation is carried out for four different cases corresponding to mass flow rates of $10\,\mu g/s$, $20\,\mu g/s$, $30\,\mu g/s$, and $40\,\mu g/s$ respectively. For each of these mass flow-rates, we consider three shutter configurations: a) $g = 5\,\mu m$, $w = 10\,\mu m$, b) $g = 2.5\,\mu m$, $w = 15\,\mu m$, c) $g = 1\,\mu m$, $w = 15\,\mu m$, and d) $g = \infty\,\mu m$ (no shutter). H_2O with molar mass of $18.015\,g/mol$, molecular mass of $2.99 \times 10^{-26}\,kg$, 3 rotational degrees of freedom, constant rotational relaxation number of 5, molecular diameter of $6.2 \times 10^{-10}\,m$, viscosity index of 1.0, and VSS scattering index of 1.0, at the

reference temperature of 273.15 K is taken as the working gas.

Verification

To verify the simulation parameters and the imposed boundary conditions, given the density and velocity of the flow, we compute the mass flow rates at three stations along the inlet. The numerical mass flow-rate is quantified by carrying out a numerical integration $\int \rho\, v\, \mathrm{d}x$ along the inlet width, where ρ, and v denote density, and y-velocity respectively. The three stations located at $Y = 0\,\mu m$, $Y = 10\,\mu m$, and $Y = 20\,\mu m$, have been indicated by thick blue line in the schematic (4). We want to emphasize that in order to get the correct mass flow rate, assuming that the integration is performed using the mid-point rule, the cells need to be refined in the inlet and near-shutter region.

TABLE 3: Nominal and DSMC flow rates. The DSMC flow rate is measured along $Y = 20\,\mu m$.

Flow rate $\dot{m}$ $(\mu g/s)$	Case 1	Case 2	Case 3	Case 4
Nominal	10	20	30	40
DSMC (without shutter)	9.7	19.5	29.3	39
$\approx$ % error in $\dot{m}$	3	2.5	2.3	2.5

Table (3) presents the mass flow-rate for different mass flow-rate conditions without shutter in place. The DSMC flow rate is measured along $Y = 20\,\mu m$. For all the four cases, the numerically estimated mass flow is within $\approx 3\%$ of the nominal mass flow-rates. We attribute the differences in flow rates to a) numerical integration error due to use of mid-point rule, b) we use 150x350 cells in the throat section: refining the grid should further lower the differences, however the same remains elusive from a computational viewpoint.

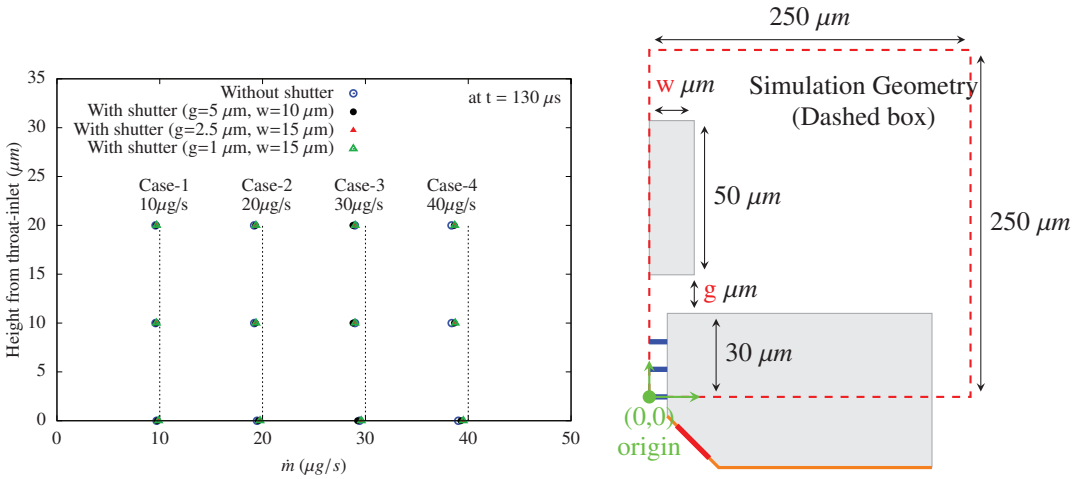

FIGURE 4: Nominal and numerical/DSMC flow rates for different geometric configurations. For verification, the DSMC mass-flow rate is measured at three y-stations (indicated by thick blue line) along the inlet.

Figure (4) illustrates the nominal and numerical/DSMC flow rates for different geometric configurations at three y-stations (indicated by thick blue line) along the inlet. We observe that the numerical flow rate approximately stays constant at different stations thereby verifying that the numerical parameters/methodology employed in the present simulations are appropriate.

Flow properties

In the present section, the flow-fields for various flow properties have been illustrated. For each of these contours, the left half ($X \leq 0$) shows the flow field for the case when the shutter is not in place ($g \to \infty$), and the right half ($X \geq 0$) shows the flow field when the shutter is in place ($0 \leq g \leq 250\,\mu m$, $0 \leq w \leq 250\,\mu m$).

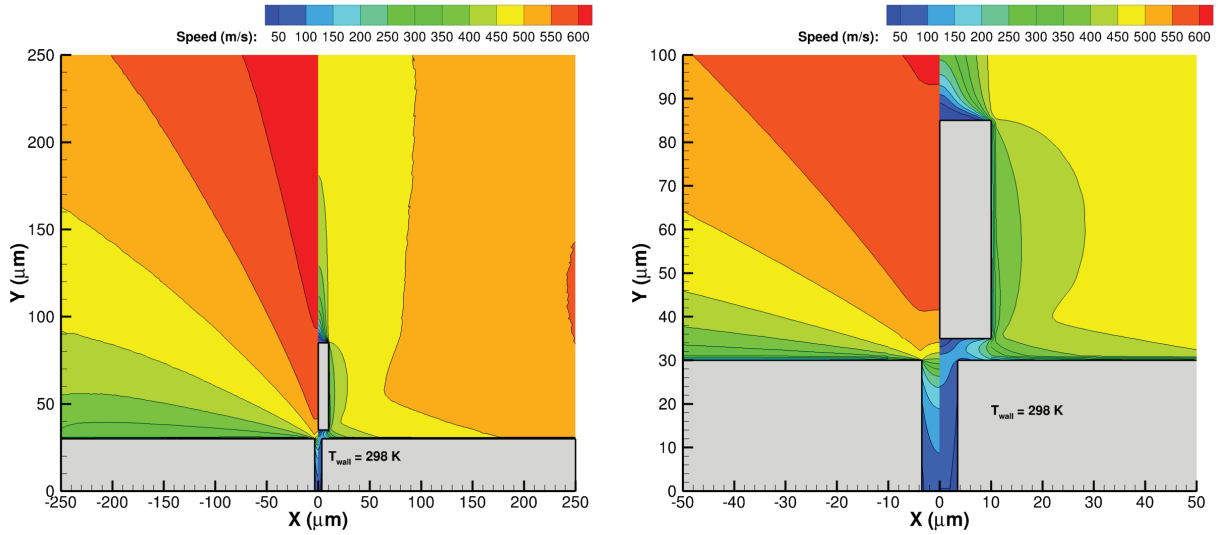

FIGURE 5: Contour of flow speed in the domain interior obtained for $\dot{m} = 10\mu g/s$, $g = 5\mu m$, $w = 10\mu m$: a) full flow field, and b) zoomed view

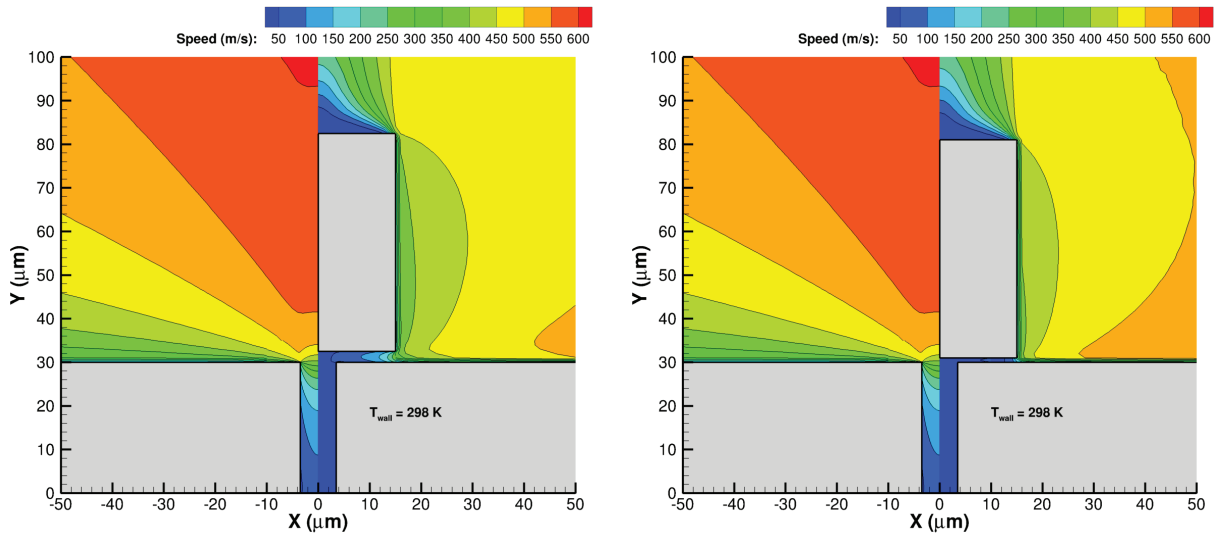

FIGURE 6: Contour of flow speed in the domain interior obtained for a) $\dot{m} = 10\mu g/s$, $g = 2.5\mu m$, $w = 15\mu m$, b) $\dot{m} = 10\mu g/s$, $g = 1\mu m$, $w = 15\mu m$.

Figures (5a, 5b) illustrate the flow speed for $\dot{m} = 10\mu g/s$, $g = 5\mu m$, $w = 10\mu m$ configuration. Without shutter in place, we observe a rapid flow expansion with centerline ($X = 0$) flow speeds acquiring values as high as 600 m/s. With shutter in place, the flow-speed along centerline ($X = 0$) is approximately 150 m/s lower. Specifically in Fig. (5b), we observe a similar flow expansions in two constrictions: ($-3.5\,\mu m \leq X \leq 0\,\mu m,\ 20\,\mu m \leq Y \leq 30\,\mu m$) and ($0\,\mu m \leq X \leq 5\,\mu m,\ 30\,\mu m \leq Y \leq 35\,\mu m$). When the gap size is decreased to $g = 2.5\,\mu m$, and the half shutter-width is increased to $w = 15\,\mu m$, the flow-speed along centerline ($X = 0$) is approximately 250 m/s lower as is also evident through Fig. (6a). When the gap size is further decreased to $g = 1\,\mu m$, keeping the same half shutter-width

($w = 15\,\mu m$), the flow-speed along centerline ($X = 0$) is approximately 300 m/s lower as is also evident through Fig. (6b).

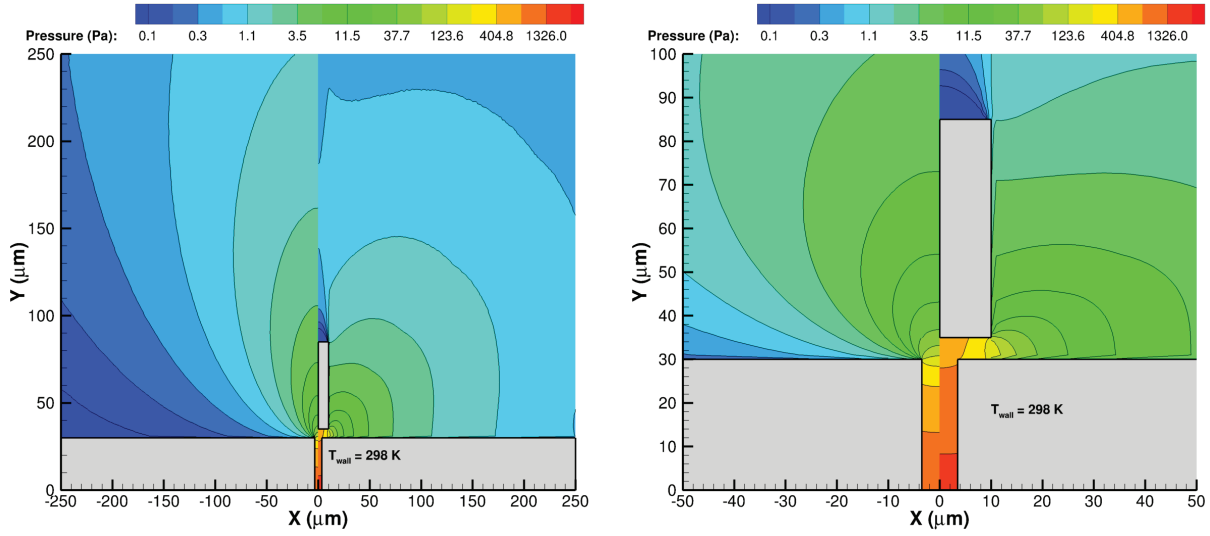

(a) (b)

FIGURE 7: Contour of flow pressure in the domain interior obtained for $\dot{m} = 10\mu g/s$, $g = 5\mu m$, $w = 10\mu m$: a) full flow field, and b) zoomed view

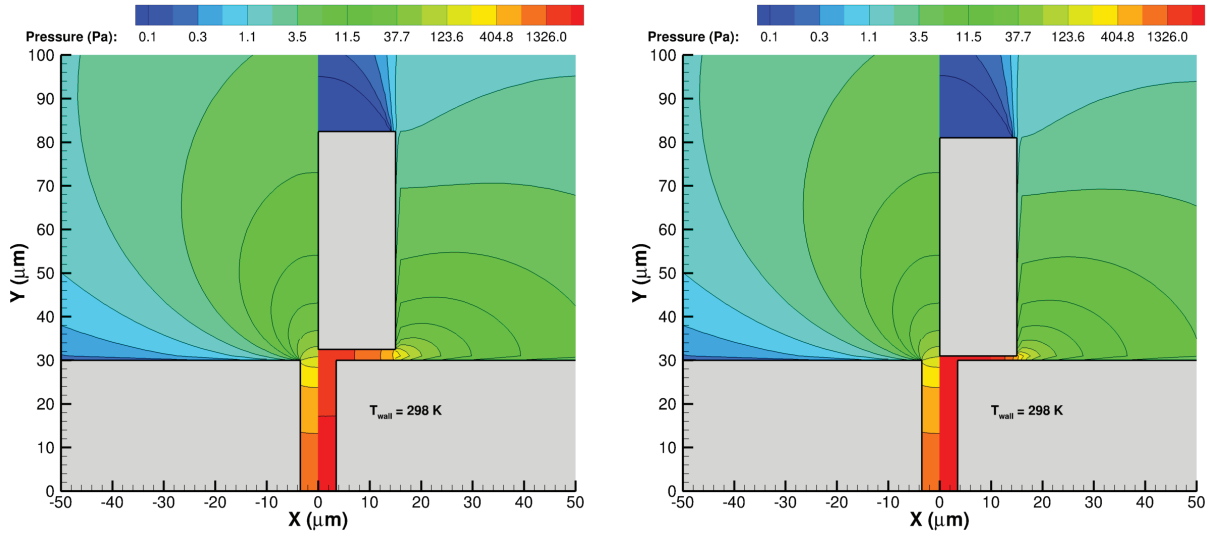

(a) (b)

FIGURE 8: Contour of flow pressure in the domain interior obtained for a) $\dot{m} = 10\mu g/s$, $g = 2.5\mu m$, $w = 15\mu m$, b) $\dot{m} = 10\mu g/s$, $g = 1\mu m$, $w = 15\mu m$.

Figures (7a, 7b) illustrate the flow pressure for $\dot{m} = 10\mu g/s$, $g = 5\mu m$, $w = 10\mu m$ configuration. Without shutter in place, we observe a rapid flow expansion (almost in form of a spiral shape with spiral's origin at the throat exit) with pressure reaching as low as 0.1 Pa. With shutter in place, the flow-pressure near the throat is approximately two times lower. In Fig. (7b), we observe a similar flow expansions in two constrictions: $(-3.5\,\mu m \leq X \leq 0\,\mu m,\ 20\,\mu m \leq$

$Y \leq 30\,\mu m$) and ($0\,\mu m \leq X \leq 5\,\mu m,\ 30\,\mu m \leq Y \leq 35\,\mu m$). When the gap size is decreased, the flow pressure increases sharply as is also evident through Figs. (8a,8b).

Back pressure

It is imperative that one can decrease the shutter gap to $\approx 0\,\mu m$ in order to completely stop the quiescent state evaporation. However, the back-pressure should decrease with decrease in gap size. A high back-pressure will interfere with system's overall lifespan. There's a trade-off between flow-evaporation rate and back-pressure in the present scenario.

Figure (9) illustrates the variation of mass flow rate and back pressure for different geometric configurations. First, we observe that the mass flow rate increases with increase in back-pressure. Second, the back-pressure increases nearly exponentially with decrease in gap-size. For gap-size of $1\,\mu m$, the back-pressure is nearly 10 times higher than the corresponding configuration with gap-size of $2.5\,\mu m$. The correlation indicated in Fig. (9) should improve with more data points.

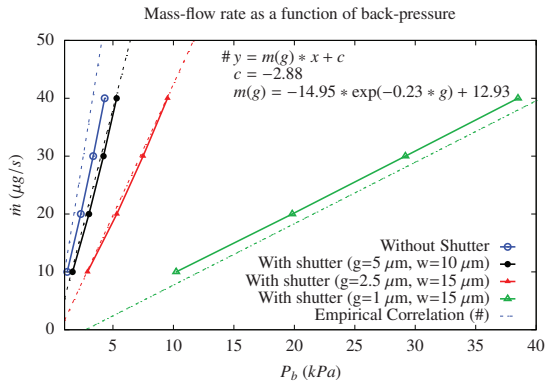

Back-pressure P_b (kPa)	Case 1	Case 2	Case 3	Case 4
Without shutter	1.22	2.34	3.37	4.32
$(g,\ w) = (5,\ 10)\ \mu m$	1.66	3.02	4.22	5.31
$(g,\ w) = (2.5,\ 15)\ \mu m$	2.90	5.32	7.49	9.51
$(g,\ w) = (1,\ 15)\ \mu m$	10.22	19.82	29.18	38.49

FIGURE 9: Variation of back-pressure for different flow rate and geometric configurations.

Condensation

From the classical nucleation theory (CNT), the condensation pressure for the onset of nucleation is given by

$$P_c = P_\infty \exp(2\sigma m/\rho_c k T_c r) \tag{1}$$

where m, ρ_c, k, P_∞, T_c, P_c, σ, and r denote the molecular mass of particle, liquid density, Boltzmann constant, flat surface pressure, condensation temperature, condensation pressure, surface tension, and radius of cluster respectively. If the pressure is greater than the condensation pressure and saturation pressure, there is a possibility of nucleation (see [22, 23, 24] and references therein).

Figure (10) shows the variation of pressure and temperature along the centerline ($X = 0$) without shutter in place for $\dot{m} = 40\,\mu g/s$ – the case with highest pressure as can be inferred from Fig. (9). Since the stream H_2O pressure is below the condensation pressures assuming ice-cluster sizes of 1 *nm* and 100 *nm*, and the saturation vapor pressure of water, the first-order approximation from CNT shows minimum possibility of condensation.

Plume Contamination

CubeSat plume expansion and impingement are important operational considerations. Although water vapor is not a benign propellant from the contamination point of view, quantifying plume interaction effects on thrust and moment is important for dynamics. The plumes from micro-thrusters may interact with free-stream as well as with each other. In practice, this situation is even more complex given the fact the CubeSat undergoes six degrees-of-freedom movement [14].

In the present case, we consider a simplified two-dimensional approximation of the plume contamination problem. Consider the top view of CubeSat as shown in Fig. (2). From a simulation point of view, the schematic of the 2-D problem has been illustrated in Fig. (11). The CubeSat, with a dimension of $100mm \times 100mm \times 100mm$, contains

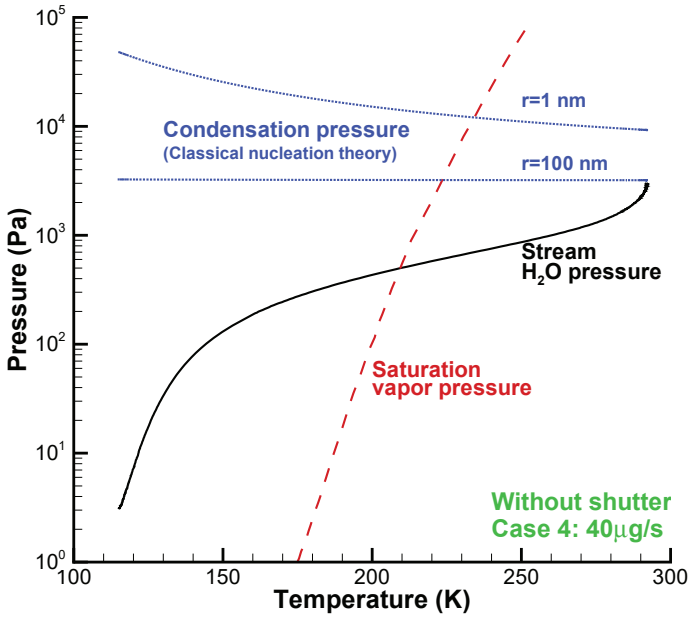

FIGURE 10: Variation of pressure and temperature along the centerline without shutter in place for $\dot{m} = 40\,\mu g/s$ – case with highest pressure as evident from Fig. (9).

four thrusters mounted at approximately 45° to each wall. At a given instant, two of the four thrusters are actuated: a) top and bottom producing a clockwise rotation perpendicular to the viewing plane, and b) left and right producing a counter-clockwise rotation perpendicular to the viewing plane. In the present work, we will consider the case when the top and the bottom thrusters are activated, and the left and right thrusters are in quiescent states with shutter in place.

Quantity	Value	Quantity	Value
Altitude, (km)	0	Free-stream mean-free path, λ_∞ (km)	32
Free-stream velocity, V_∞, (km/s)	7.66	Mean collision time, (sec)	50
Free-stream temperature, T_∞, (K)	787	Domain cells	750×750 (adaptive)
Working Fluid	H_2O (jet)		
	O+N_2+He (free-stream)	Domain extent, (m)	15×15 m
	3.45e+13 (O)	Jet velocity, V_{jet} (m/s)	591.95
Number density, n_∞, (m^{-3})	7.615e+11 (N_2)	Jet temperature, $T_{\text{jet}}(K)$	298
	8.20e+12 (He)	Jet number density, n_{jet} (m^{-3})	5.1656e+23
	0.787 (O)	Jet mean-free path, λ_{jet} (m)	2×10^{-6}
Number fraction	0.0174 (N_2)		
	0.187 (He)		

TABLE 5: Case parameters for quantification of plume contamination.

The DSMC simulation parameters have been indicated in the Tab. (1). At CubeSat walls, we use fully diffuse surface boundary condition. At the right, top and bottom free-stream boundaries, the outlet boundary condition has been used. At the left boundary, an inlet boundary condition is imposed with gas molecules entering with V_∞ with the specified number density n_∞, and temperature T_∞. The thruster plumes are modeled using an inlet boundary condition with gas molecules entering with V_{jet} with the specified number density n_{jet}, and temperature T_{jet}.

The simulation domain $15\,m \times 15\,m$ is first discretized uniformly using 750×750 cell Cartesian-grid. Due to large difference in the free-stream and thruster's number density, we employ an adaptive grid. The grid is adapted so that every cell has at least 20 particles. H_2O is taken as the working gas for thruster plumes. The VSS model parameters for

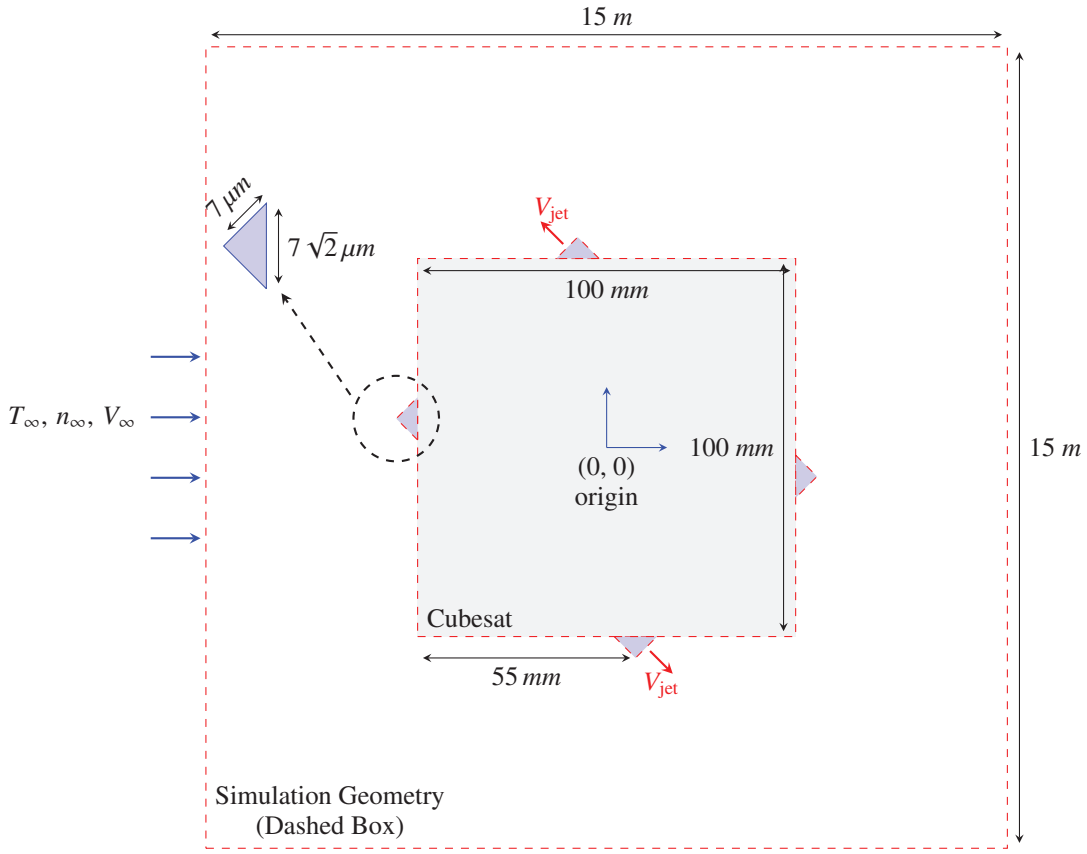

FIGURE 11: Schematic for quantification of plume contamination.

H_2O remain the same as in the quiescent evaporation problem except that we use reference diameter of $5.8 \times 10^{-10}\, m$ in the present case. It is worth noting that both the reference diameters of ~ 5.8Å[25] and 6.2Å[26] have been used in previous DSMC studies. The VSS model parameters for the free-stream containing approximately 78.7% O, 1.74% N_2, and 18.7% He use the parameters from [8].

Figure (12a) illustrates the variation of flow speed in the near CubeSat region. As expected, the flow speeds are highest along the 45° – the direction of thruster plumes. Near the left and right walls, we observe blue triangular regions which are due to the flow turning around the corners commonly identified as Prandtl Meyer expansions.

Figure (12b) illustrate the variation of pressure in the near CubeSat region. We observe that the plume rapidly expands into the vacuum with pressures dropping down by 3 orders of magnitude. The left and right walls are in shadow regions, and are therefore largely unaffected by the plumes from top and bottom thrusters.

Figure (13) depicts the variation of number flux on all four walls of the CubeSat. The number of particles colliding per unit surface area is highest around the location of thrusters on both top and bottom walls. Away from the thruster locations, the concentration drops exponentially. The left and right walls are largely unaffected by the plumes from the thrusters located at the top and bottom walls. For the top jet directed towards north west, we observe large deposition in the left half of the top CubeSat wall, and smaller deposition in the right half of the top CubeSat wall. For the bottom jet directed towards south east, we observe large deposition in the right half of the bottom CubeSat wall, and smaller deposition in the left half of the bottom CubeSat wall. This unbalance should affect the moment due to uneven plume deposition. The quantification of this uneven plume deposition, and its net effect on CubeSat's moment characteristics is subject of future study.

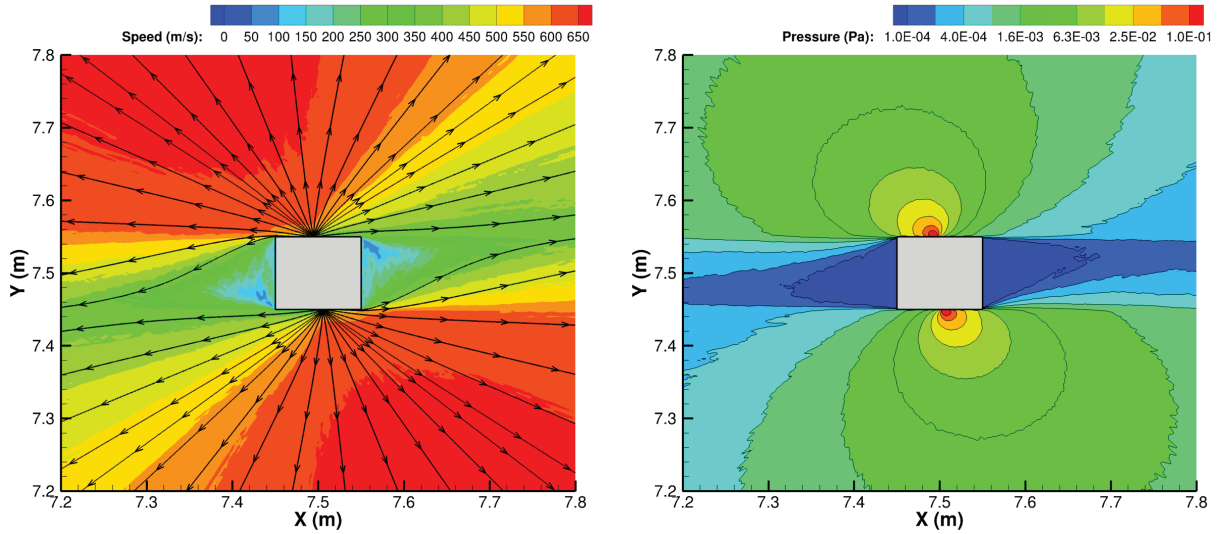

(a) (b)

FIGURE 12: Variation of flow properties in the near CubeSat region: a) speed, and b) pressure.

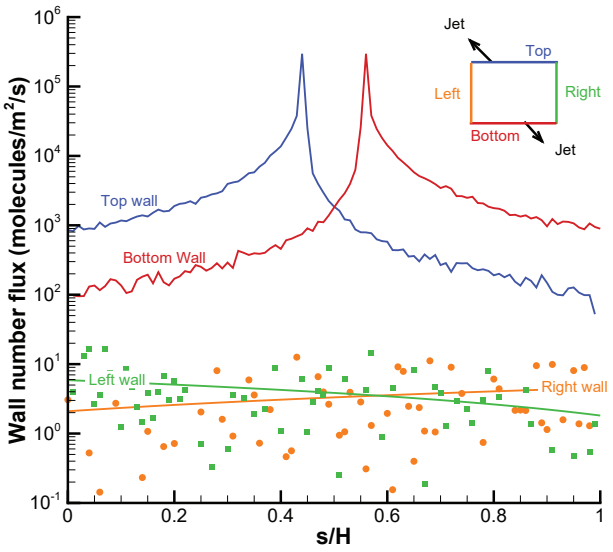

FIGURE 13: Number flux on all four walls of the CubeSat. Here s denotes the length along the wall. For the left and the right walls $s = y$, and for the top and the bottom walls $s = x$.

CONCLUSIONS

The evaporation rate of FEMTA micro-propulsion system in quiescent system state is quantitatively characterized using DSMC method. With shutter in place, flow speed decreases by as much as 300 m/s. The DSMC results further indicate the mass flow rate decreases nearly exponentially by decreasing the shutter-gap (g) and increases linearly by increasing the half shutter-width (w). A preliminary estimate from CNT suggests minimum possibility of condensation as the vapor exits from the thrusters. The plume contamination studies suggest that the water-vapor is largely deposited around the location of thrusters. Away from the thrusters, the concentration on walls drops exponentially. While the results from the present work are indeed promising, the future work will likely address the plume contamination subject to changes in geometric configurations. The full scale 3D simulations with cross-plume interactions is yet

another interesting direction of future work.

Acknowledgment

Development of the FEMTA micro-propulsion technology is supported by NASA SmallSat Technology Partnership program under NNX15AW40A and NNX18035512 in collaboration with NASA Goddard Space Flight Center.

REFERENCES

[1] C. Sultan, S. Seereram, and R. K. Mehra, The International Journal of Robotics Research **26**, 405–430 (2007).
[2] R. Wirz, J. Mueller, M. Gale, and C. Marrese, "Miniature ion thruster for precision formation flying," in *40th AIAA/ASME/SAE/ASEE Joint Propulsion Conference and Exhibit* (2004) p. 4115.
[3] N. Warner and M. Martinez-Sanchez, "Design and preliminary testing of a miniaturized TAL Hall thruster," in *42nd AIAA/ASME/SAE/ASEE Joint Propulsion Conference & Exhibit* (2006) p. 4994.
[4] M. Tajmar, A. Genovese, and W. Steiger, Journal of propulsion and power **20**, 211–218 (2004).
[5] D. L. Hitt, C. M. Zakrzwski, and M. A. Thomas, Smart Materials and Structures **10**, p. 1163 (2001).
[6] W. Stein, A. Alexeenko, and I. Hrbud, Journal of Propulsion and Power **24**, 1007–1017 (2008).
[7] A. G. Cofer, W. O'neill, A. Alexeenko, S. D. Heister, and E. H. Cardiff, "Film-evaporation MEMS Tunable Array: Theory of Operation and Proof of Concept," in *50th AIAA/ASME/SAE/ASEE Joint Propulsion Conference* (AIAA, 2014) p. 3855.
[8] G. A. Bird, *Molecular Gas Dynamics and the Direct Simulation of Gas Flows* (Clarendon Press, Oxford, 1994).
[9] M. Ivanov and S. Gimelshein, Annual Review of Fluid Mechanics **30**, 469–505 (1998).
[10] W. J. O'Neill, A. G. Cofer, A. B. Weaver, and A. Alexeenko, "Heat and mass transfer analysis of a film evaporative MEMS tuneable array thruster," in *45th AIAA Thermophysics Conference* (AIAA, 2015) p. 2352.
[11] A. Strongrich, A. Pikus, I. B. Sebastião, and A. Alexeenko, Journal of Microelectromechanical Systems **26**, 528–538 (2017).
[12] D. Parkos, A. Alexeenko, M. Kulakhmetov, B. C. Johnson, and H. J. Melosh, Journal of Geophysical Research: Planets **120**, 2152–2168 (2015).
[13] A. G. Cofer, W. J. O'Neill, S. D. Heister, A. Alexeenko, and E. H. Cardiff, "Film-evaporation MEMS tunable array for low-mass SmallSat propulsion: design improvements and thrust characterization," in *51st AIAA/SAE/ASEE Joint Propulsion Conference* (AIAA, 2015) p. 3993.
[14] K. Fowee, S. Pugia, M. Linker, M. Fuehne, R. Clay, A. Cofer, and A. Alexeenko, "Quad-thruster FEMTA micropropulsion system for cubesat 1-axis control," in *31st Annual AIAA/USU Conference on Small Satellites* (2017).
[15] M. A. Gallis, J. R. Torczynski, S. J. Plimpton, D. J. Rader, T. Koehler, and J. Fan, "Direct simulation Monte Carlo: The quest for speed," in *AIP Conference Proceedings*, Vol. 1628 (AIP, 2014), pp. 27–36.
[16] M. A. Gallis, N. P. Bitter, T. P. Koehler, J. R. Torczynski, S. J. Plimpton, and G. Papadakis, *Physical Review Letters*, **118**, p. 064501 (2017).
[17] M. A. Gallis, T. P. Koehler, J. R. Torczynski, and S. J. Plimpton, *Physical Review Fluids*, **1**, p. 043403 (2016).
[18] C. Pekardan and A. Alexeenko, AIAA Journal 765–779 (2017).
[19] I. B. Sebastiao, L. Qiao, and A. A. Alexeenko, *Combustion and Flame*, **198**, 40–53 (2018).
[20] S. Jaiswal, A. A. Alexeenko, and J. Hu, Journal of Computational Physics **378**, 178–208 (2019).
[21] S. Jaiswal, I. Sebastião, and A. A. Alexeenko, "DSMC-SPARTA Implementation of M-1 Scattering Model," in *31st Rarefied Gas Dynamics Symposium* (AIP, 2018).
[22] P. Hill, H. Witting, and E. Demetri, Journal of Heat Transfer **85**, 303–314 (1963).
[23] R. Kung, L. Cianciolo, and J. Myek, AIAA Journal **13**, 432–437 (1975).
[24] A. Borner, Z. Li, and D. A. Levin, The Journal of chemical physics **138**, p. 064302 (2013).
[25] A. A. Alexeenko, A. Ganguly, and S. L. Nail, Journal of pharmaceutical sciences **98**, 3483–3494 (2009).
[26] R. Jansen, I. Wysong, S. Gimelshein, M. Zeifman, and U. Buck, The Journal of chemical physics **132**, p. 244105 (2010).